

ATMOSPHERIC TURBULENCE MODELING AND IMPLICATIONS FOR WIND ENERGY

Fotini Katopodes Chow and Bowen Zhou

Civil and Environmental Engineering, University of California, Berkeley, USA

tinakc@berkeley.edu

Abstract

The near-surface structure of atmospheric turbulence affects the design and operation of wind turbines and is especially difficult to predict under stably-stratified conditions. The stably-stratified boundary layer can lead to low-level jets, with strong vertical shear, and intermittent turbulence that can affect turbine lifetimes and performance. On the other hand, increased wind speeds in the low-level jet may provide untapped resources for wind power extraction. This study uses large-eddy simulation (LES) to explore properties of the stably-stratified atmospheric boundary layer using an explicit filtering and reconstruction approach with a finite difference method. The structure of the stable boundary layer (SBL) and turbulence statistics reach general agreement with well-established similarity theories, even at relatively coarse resolution. Traditional closure models perform poorly in comparison. Subfilter-scale dissipation and backscatter events are statistically characterized, showing the ability of this turbulence modeling framework to allow for energy exchange from small to large scales. A low-level jet (LLJ) develops in the simulations, and wind shear in the jet is responsible for generating additional turbulent kinetic energy (TKE) around the top of the boundary layer. This elevated TKE is unexpected based on previous modeling results with traditional turbulence closures, but is in agreement with field observations under certain conditions. The explicit filtering and reconstruction framework is thus able to correctly capture atmospheric dynamics that do not conform to traditional assumptions of gradient-diffusion turbulence models and may be of particular use in wind energy applications under stable conditions.

1 Introduction

Wind turbines sit at the very bottom of the atmospheric boundary layer, where winds are highly turbulent, shear events are intermittent, and land-atmosphere interactions may be strong. Turbine hub heights have increased over the years to now be between 80 and 120 m above ground level, with blade diameters of 80-120 m. Current operational practices for wind farm operation and siting rely on power law esti-

mates for the wind speed variation with height and assume neutral stratification. Similarly, practical guidelines for impacts of turbulence and shear on turbines are based on theoretical estimates for idealized flows. Thus, wind farm operators may be overly conservative and reduce power production by turning turbines off too early in high winds, or may risk severe damage to the rotors and blades by operating under conditions that lead to excess fatigue, depending on the prevailing atmospheric conditions.

High-resolution simulations of atmospheric flow are currently being developed to provide predictions for wind turbine micrositing and operational wind power forecasting. For example, Palma et al. (2008) used numerical simulations to examine the vertical structure of turbulence and wind shear at a coastal wind farm and found many atmospheric conditions violated the design criteria for turbine operation (turbulence intensity too high or wind shear too high). Large-eddy simulation (LES), in particular, has shown promise for application to wind energy because it can adequately resolve turbulent flow in the lowest few hundred meters of the atmospheric boundary layer (ABL). LES is based on the definition of a spatial filter which can be adjusted to resolve necessary flow features. The spatial filter separates the large resolved scales from the subfilter-scale (SFS) motions. The effect of SFS scales on the resolved scale must be represented with a turbulence model. Basu et al. (2008) simulated a full diurnal cycle with LES, focusing on boundary layer transitions, showing the predictive capabilities of LES specifically with wind energy applications in mind. Several recent studies have used LES over isolated hills to examine turbulence structure with applications to wind energy (Bechmann and Sorensen, 2010; Calaf et al., 2010; Paiva et al., 2009; Chow and Street, 2009).

One of the greatest current challenges in applying LES to wind energy lies in the representation of turbulence in the ABL, which is strongly affected by the stability of the atmosphere. The stable boundary layer (SBL) occurs nearly every night over land and is often complicated by low-level jets, inertial oscillations, and gravity waves. In the Southern Great Plains region of the United States, for example, low-level jets (LLJs) occur regularly at night and represent a large untapped wind resource (due to higher wind speeds)

but also a hazard for turbine operation due to strong vertical shear and turbulence (Sisterson and Frenzen, 1978). Turbine failures and fatigue show strong correlation to high wind shear and turbulence intensity (Kelley et al., 2006). Storm et al. (2009) used the Weather Research and Forecasting mesoscale atmospheric model to study LLJs over the Southern Great Plains for wind forecasting purposes. They found that while WRF tended to overestimate the LLJ height and underestimate the LLJ wind speeds, predictions were much improved over standard power law relations.

In this work we focus on simulations of the stably-stratified boundary layer which occurs most nights over land and which generates favorable winds for wind power extraction in some regions of the world. The main challenge in simulating stably-stratified conditions is that the length scale of turbulent eddies in the atmospheric boundary layer is much smaller than under convective or neutral conditions, thus requiring higher grid resolution in numerical simulations. Previous numerical simulations of the SBL have been limited to mild stability, with conditions of either high geostrophic forcing or low surface cooling rate (Saiki et al., 2000; Basu and Porté-Agel, 2006). Both conditions result in turbulence profiles within the continuous regime. As stability increases, spatially and temporally intermittent turbulence can develop and eddy sizes are strongly damped. Under these conditions, resolved turbulent stresses diminish quickly if the SFS model is not carefully chosen to sustain intermittent turbulence.

We use the dynamic reconstruction turbulence model of Chow et al. (2005) for SBL simulations. This turbulence model applies an explicit filtering and reconstruction approach that is different from traditional eddy-viscosity closures. This dynamic reconstruction model (DRM) has previously been shown to be advantageous in turbulent channel flow (Gullbrand and Chow, 2003) and in neutral ABL simulations (Chow et al., 2005). In contrast to traditional eddy-viscosity closures, the explicit filtering and reconstruction model possesses many promising features for simulating the SBL, as described below. One major advantage is that almost any existing SFS model can be adapted to an explicit filtering and reconstruction framework.

The Advanced Regional Prediction System (ARPS) (Xue et al., 2000) is used for the simulations. ARPS is a non-hydrostatic mesoscale and small-scale LES finite difference model. The code has been adapted to accommodate the new DRM SFS closure using the explicit filtering and reconstruction framework (Chow et al., 2005). We will demonstrate superior agreement of the dynamic reconstruction model with similarity theory, compared to standard LES closures for SBL simulations. We consider strong surface cooling that places the boundary layer turbulence at the threshold of the continuous regime,

as well as two cases where turbulence is intermittent in nature. We specifically focus on the vertical structure of mean winds and turbulence in the SBL which is of interest in wind energy applications.

2 Governing equations

The traditional approach towards LES has been to treat the discrete differentiation operation as an implicit filter to separate large from small scales in the governing equations. With finite volume and finite difference approaches, implicit filtering can lead to truncation and aliasing errors (Lund, 1997) due to the nonlinear terms. Here we adopt the explicit filtering approach of Gullbrand and Chow (2003) that was applied to the ABL by Chow et al. (2005). A 3D explicit filter (typically a tophat filter of width Δ twice the grid spacing) is applied to the Navier-Stokes equations, and is treated separately from the numerical differencing operators. The implicit discretization operator is denoted by a tilde and the explicit filtering operator by a bar. Explicit filtering of the nonlinear terms can minimize the influence of truncation errors and has been shown to be beneficial in recent studies (e.g. Gullbrand and Chow, 2003). In our notation, the tilde operator is a loose representation of the implicit filter operation, and its nature depends on the discrete differentiation schemes whose effects cannot usually be exactly characterized. The LES governing equations for the resolved fields are the momentum, continuity, and scalar transport equations:

$$\begin{aligned} \frac{\partial \bar{\rho} \bar{u}_i}{\partial t} + \frac{\partial \bar{\rho} \bar{u}_i \bar{u}_j}{\partial x_j} &= -\frac{\partial \bar{p}}{\partial x_i} - \bar{\rho} g \delta_{i3} + \bar{\rho} \epsilon_{imn} f_n \bar{u}_m - \frac{\partial \bar{\rho} \bar{\tau}_{ij}}{\partial x_j} \\ \frac{\partial \bar{\rho}}{\partial t} + \frac{\partial \bar{\rho} \bar{u}_i}{\partial x_i} &= 0 \\ \frac{\partial \bar{\theta}}{\partial t} + \frac{\partial \bar{\rho} \bar{u}_i \bar{\theta}}{\partial x_i} &= -\frac{\partial \bar{\rho} \bar{\chi}_i}{\partial x_i} \end{aligned}$$

where \bar{u}_i are the velocity components, \bar{p} the pressure, $\bar{\rho}$ the density, f the Coriolis parameter, and $\bar{\theta}$ the potential temperature. The turbulent stresses and heat fluxes are defined as follows and can be decomposed into resolvable subfilter-scale (RSFS) stresses and unresolvable subgrid-scale (SGS) stresses:

$$\begin{aligned} \tau_{ij} &= \overline{u_i u_j} - \bar{u}_i \bar{u}_j = \underbrace{(\overline{u_i u_j} - \bar{u}_i \bar{u}_j)}_{\tau_{SGS}} + \underbrace{(\bar{u}_i \bar{u}_j - \bar{u}_i \bar{u}_j)}_{\tau_{RSFS}} \\ \chi_i &= \overline{u_i \theta} - \bar{u}_i \bar{\theta} = \underbrace{(\overline{u_i \theta} - \bar{u}_i \bar{\theta})}_{\chi_{SGS}} + \underbrace{(\bar{u}_i \bar{\theta} - \bar{u}_i \bar{\theta})}_{\chi_{RSFS}} \end{aligned}$$

The first set of parentheses on the right-hand side contains the SGS stresses, τ_{SGS} , which represent the difference between the total and resolved stress components and must be modeled. The second set of parentheses contains the filtered-scale stresses, τ_{RSFS} ,

which depend on the resolved and explicitly filtered velocity fields within the resolution domain. As the explicit filter function is well defined, it is theoretically possible to obtain \tilde{u}_i from \bar{u}_i and $\tilde{\theta}$ from $\bar{\theta}$ by deconvolution (inverse filtering).

The RSFS/SGS model framework can be viewed in terms of a mixed model (Bardina et al., 1983; Zang et al., 1993). The RSFS piece is the so-called ‘‘scale similarity’’ term represented by reconstruction, and the SGS piece is represented using an eddy-viscosity closure. With zero-level reconstruction, the RSFS term reduces exactly to the scale similarity model of Bardina. With higher levels of reconstruction, more details of high frequency motions approaching the grid cutoff are restored, thus improving the representation of the SFS stress. Using the same approach, Chow et al. (2005) performed simulations of the neutral boundary layer which reproduced the expected logarithmic velocity profile and better represented turbulent stresses.

3 Explicit filtering and reconstruction turbulence modeling framework

RSFS reconstruction model

Reconstruction of the RSFS stress is accomplished through the approximate deconvolution method (ADM) (Stolz et al., 2001). The unfiltered quantity can be reconstructed in an iterative fashion by successive filtering operations (G) applied to the filtered quantities:

$$\tilde{u}_i = \bar{u}_i + (I - G) * \tilde{u}_i + (I - G) * [(I - G) * \tilde{u}_i] + \dots \quad (1)$$

where I is the identity operator, G is the explicit filter, and ‘ $*$ ’ is the convolution operator. Higher order of accuracy can be achieved by including more terms in the series expansion, simply by repeated application of the same filtering operation.

The RSFS term is computed by substituting the reconstructed velocity (\tilde{u}_i^*) into the τ_{RSFS} term (i.e. $\tau_{RSFS} = \overline{\tilde{u}_i^* \tilde{u}_j^*} - \bar{u}_i^* \bar{u}_j^*$). In this work, up to five levels of reconstruction are applied to enhance the role of the RSFS stresses. More details can be found in Chow et al. (2005).

SGS turbulence and wall models

Reconstruction of the RSFS stress is only able to capture motions up to the Nyquist grid cutoff, thus the SGS model must represent any motions smaller than the grid spacing. We apply the Wong and Lilly (1994) dynamic eddy-viscosity model to represent SGS motions:

$$\tau_{SGS} = -2\nu_T \bar{S}_{ij},$$

where $\bar{S}_{ij} = (\partial \bar{u}_i / \partial x_j + \partial \bar{u}_j / \partial x_i) / 2$ is the resolved strain rate tensor, and the dynamic eddy viscosity, ν_T , is given by $\nu_T = C_\epsilon \Delta^{4/3}$. The coefficient C_ϵ is determined using the least-squares method of Lilly (1992).

Further details of the dynamic eddy viscosity calculations using explicit filtering are explained in Chow et al. (2005). For comparison with the traditional LES approach, the static Smagorinsky model and the TKE-1.5 model are also used (standard closures in ARPS).

Because the near-wall stresses are usually under-predicted with dynamic SGS models applied in ABL flows, a near-wall stress model must be applied to improve the near wall stress profile (Chow et al., 2005; Brown et al., 2001). Modifications to the near-wall turbulence closure are common even for non-dynamic closures (see e.g. Sullivan et al., 1994). The near-wall stress is given by,

$$\tau_{i, near-wall} = - \int C_c a(z) |\tilde{u}| \tilde{u}_i dz$$

where C_c is a strength factor, and the function $a(z)$ is a shape factor to set a smooth decay of $\tau_{i, near-wall}$ to zero at the specified cutoff height h_c . Implementation of this near-wall model has proved successful in the work of Brown et al. (2001), Cederwall (2001), Chow et al. (2005), and Kirkpatrick et al. (2006).

The complete dynamic reconstruction model (Chow et al., 2005) is a mixed model for the total SFS stress consisting of the RSFS and SGS components, which are respectively scale-similarity and eddy-viscosity terms with near-wall enhancement:

$$\tau_{ij} = \underbrace{(\overline{\tilde{u}_i^* \tilde{u}_j^*} - \bar{u}_i^* \bar{u}_j^*)}_{\tau_{RSFS}} - 2C_\epsilon \Delta^{4/3} \underbrace{\bar{S}_{ij}}_{\tau_{SGS}} + \tau_{i, near-wall}. \quad (2)$$

The level of reconstruction (n) is determined by the number of terms ($n + 1$) in the series expansion in Eq. (1); for example, level-0 reconstruction includes one term in the series and is denoted DRM-ADM0. Level-0 reconstruction is similar to the mixed model of Bardina et al. (1983).

4 Model configuration

Simulations are performed on a (640 m, 640 m, 640 m) domain over flat but rough terrain. Low resolution simulations with 43^3 grid points are used to place more emphasis on the role of the turbulence model. The grid is evenly spaced horizontally and stretched vertically using a hyperbolic tangent stretching option, with a minimum spacing of 5 m near the ground. The horizontal spacing is considerably coarser (16 m) than the guidelines provided in previous studies (Beare et al., 2006). Simulations with twice the horizontal domain size (1280 m, 1280m, 640m) lead to nearly identical simulation results (not shown), thus confirming that our domain includes relevant large scale motions.

Lateral boundary conditions are periodic, and the lower boundary is set to be a rigid wall. At the top boundary, Rayleigh damping is applied above 500 m. The boundary layer height ranges from 100-200 m and thus should not be affected by the Rayleigh damping. A constant surface heat flux is imposed at -0.02

Km s^{-1} to simulate mildly stable conditions. Cooling rates from -0.03 to -0.07 Km s^{-1} are also tested for the DRM models. (The Smagorinsky and TKE-1.5 models fail to sustain resolved TKE with these cooling rates.) The surface momentum flux is prescribed by imposing Monin-Obukhov similarity at the first grid point above the ground.

The flow is driven by a geostrophic wind at $(U_g, V_g) = (10 \text{ m/s}, 0 \text{ m/s})$ and initialized using a uniform wind profile. The initial potential temperature is uniform at 300 K (neutral conditions). A random perturbation of 0.1 K is applied to the bottom 150 m of the domain at initialization to trigger turbulence.

All simulation results presented are planar averaged in the horizontal direction and time averaged over the last two hours of the simulation, unless otherwise stated.

5 Simulation results

Spin-up and quasi-steady mean profiles

All simulations (except Smagorinsky) are carried out for 14 hrs of physical time, equivalent to a dimensionless time of $tf = 5$, where f is the local Coriolis parameter. While simulations with both dynamic procedures and the TKE-1.5 model develop into a turbulent flow field when continuous surface cooling is applied, the static Smagorinsky model sees a rapid decay of resolved TKE (see Mason and Derbyshire, 1990). Therefore, for the Smagorinsky case heating is applied at a constant surface heat flux of 0.01 Km s^{-1} for the first 3 hrs before switching to cooling, for a total of 19 hrs of simulation time. It is also found that the Smagorinsky constant C_s needs to be reduced from the usual range of 0.18 - 0.20 to a value of at most 0.15 to ensure sustained resolved turbulence in the moderate cooling case.

Vertical profiles of mean wind speed and potential temperature at quasi-steady state both depend strongly on the choice of turbulence models. In the moderate cooling case, the boundary layer height ranges from about 100 m (TKE-1.5 model) to around 200 m (DRM models), also affecting wind shear and LLJ height (Fig. 1(a)). Such sensitivity is also reflected in the mean vertical potential temperature profile (Fig. 1(b)), with the TKE-1.5 model predicting much a lower surface temperature and stronger self-capping inversion strength than the DRM models. Small variabilities in the mean profiles are also observed among DRM models depending on levels of reconstruction used. In addition, large differences are observed between the predicted SBL wind profile and conventional power law relations that are used in wind energy applications: $U(z) = U_r(z/z_r)^\alpha$, where z_r and U_r are reference height and wind speed taken usually at 10 m AGL, and α is the shear exponent. Under mildly stable conditions, the best fit for α is larger than $1/7$, the typically assumed value for the NBL. It also exceeds 0.2 ,

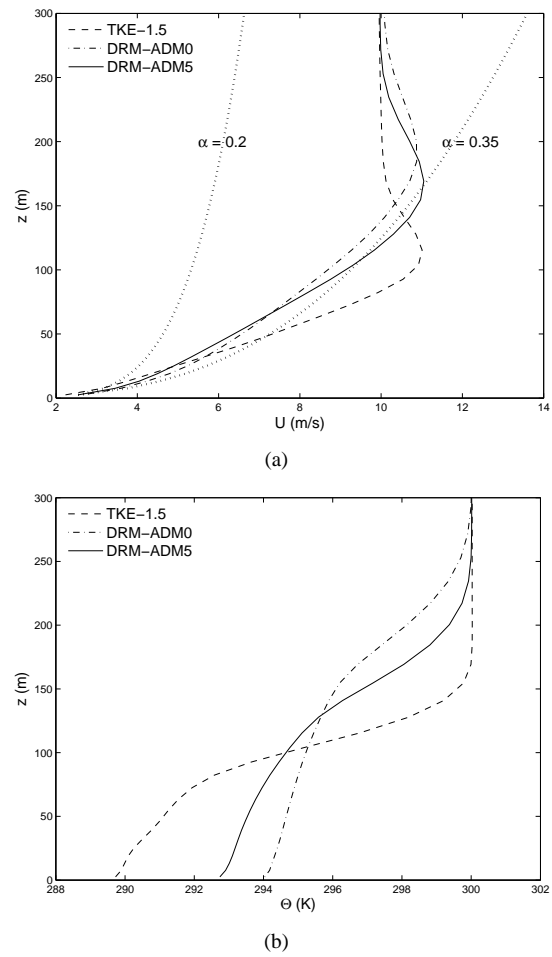


Figure 1: Mean vertical profile of (a) wind speed and (b) potential temperature, for different closure models.

the International Electronic Commission (IEC) specification value for wind turbine design, reaching nearly 0.35 (Fig. 1(a)). For stronger cooling rates, α increases further up to 0.5 . The predicted deviations from standard profiles are important for wind energy applications. Underestimation of the shear exponent often results in elongated turbine fault time (when turbines must be turned off to prevent damage from high winds or turbulence). Based on a 1-year study in the Southern Great Plains, Smith et al. (2002) showed that turbine fault time at local wind farms is highly correlated with the wind shear exponent from midnight to early morning where stable conditions prevail.

Vertical shear profiles

Monin-Obukhov (MO) similarity theory describes the vertical profiles of the SBL variables as a function of the dimensionless group z/L (where L is the Obukhov length), and is applicable in the surface region where z/L is smaller than unity. Businger et al. (1971) experimentally obtained the following relationships for the SBL using MO theory,

$$\phi_m = \frac{\kappa z}{u_*} \frac{\partial \bar{U}}{\partial z} = 1 + \beta \zeta, \quad \phi_h = \frac{z}{\theta_*} \frac{\partial \bar{\theta}}{\partial z} = 0.74 + \beta \zeta$$

where ϕ_m is the dimensionless wind shear, ϕ_h is the dimensionless temperature gradient, $\zeta = z/L$ is the dimensionless height, β is a constant equal to the inverse of the critical gradient Richardson number $R_{i,c}$, and θ_* is a generic turbulent temperature scale defined as $\theta_* = -\overline{w\theta}/\kappa u_*$.

Over the years, researchers have proposed slightly different values for the slope β ; this reflects some uncertainty in the understanding of turbulent transport mechanisms near the surface under stable conditions. In addition, the value of the intercept for ϕ_h is the subject of much debate. According to Obukhov's original derivation, the intercept takes on the value of the surface turbulent Prandtl number Pr_T . Although different values of surface Pr_T are suggested by field measurements, LES, and DNS studies, a range between 0.5 and 1 is generally accepted. The reader should also be cautioned that although MO similarity theory provides a general guideline for surface flux scaling, it is much less certain that MO theory should apply under "universal" stable conditions, particularly under strong stability (Wilson, 2008).

The performance of the explicit filtering and reconstruction model is reflected in its good agreement with the theoretical ϕ_m and ϕ_h , even at a relatively coarse horizontal resolution of 16 m (see Fig. 2). Both ϕ_m and ϕ_h produced from the Smagorinsky and TKE-1.5 model deviate much more than DRM from the MO similarity curve. In addition, the coarse resolution case with level 5 reconstruction (DRM-ADM5) does almost as good a job as the same model at higher resolution (DRM-ADM5-HR), especially near the first few grid points above the ground. In addition, when the intercept of the theoretical ϕ_h curve, or surface Pr_T , takes the value of 0.55 instead of 0.74 (as predicted by our simulations), agreement of the DRM results with MO theory on ϕ_h is comparable to that of ϕ_m . The LES study of Basu and Porté-Agel (2006) also predicts a surface Pr_T value around 0.5.

Overall, our agreement with MO similarity theory is comparable to or better than most previous LES works on the SBL (e.g. Saiki et al., 2000). This is remarkable considering that the horizontal grid resolution for the present coarse simulation is 16 m. Although we use grid stretching in the vertical direction (minimum spacing of 5 m), the average vertical resolution is still much coarser than the GABLS suggested value of 6.25 m (note that isotropic grid spacing is used in the GABLS study) to produce a moderate SBL "simulation of a reasonable (of order 20%) accuracy compared to the very high resolution simulations" (Beare et al., 2006).

SFS dissipation and backscatter

The SFS dissipation rate Π is defined in the TKE equation as, $\Pi = -\tau_{ij}\overline{S}_{ij}$, and represents the energy transport between resolved scales and subfilter scales. Unlike dissipation at the molecular level, SFS dissipation is a two way process, involving mostly transfer

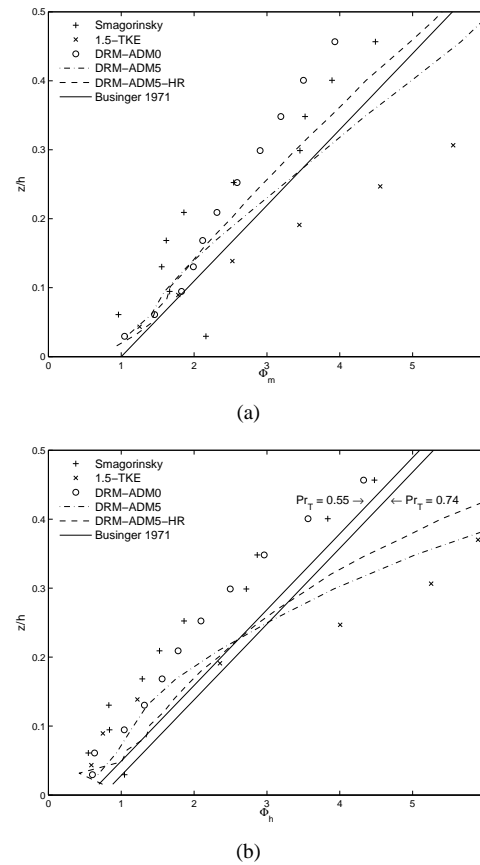


Figure 2: Vertical profiles of (a) non-dimensional shear and (b) non-dimensional potential temperature gradient for various turbulence models, compared to similarity theory. Because MO theory is only expected to hold for $\zeta < 1$, only the relevant range is presented.

of energy from the large energetic eddies into subfilter motions (positive Π values), but occasionally the reverse process, known as backscatter (negative Π values). From field data, Carper and Porté-Agel (2004) found a non-Gaussian distribution of Π with significant portions of backscatter in mildly convective and near neutral conditions.

Most canonical SFS models are deficient in capturing the right amount of dissipation, and if any at all, backscatter. Backscatter is a key mechanism in intermittent turbulence that occurs under very strong cooling; the ability to model backscatter in LES could affect predictions of intermittent high shear or turbulence events which affect wind turbine operation. Conventional eddy-viscosity models tend to over-suppress turbulence development in the SBL due to their purely dissipative nature, and flow tends to relaminarize quickly under moderately stable conditions. Dynamic eddy-viscosity models correct the over-dissipation problem, but they are still absolutely dissipative, unless some negative values are allowed for eddy viscosity (which are often problematic, Zang et al. (1993)). In contrast, scale similarity models natu-

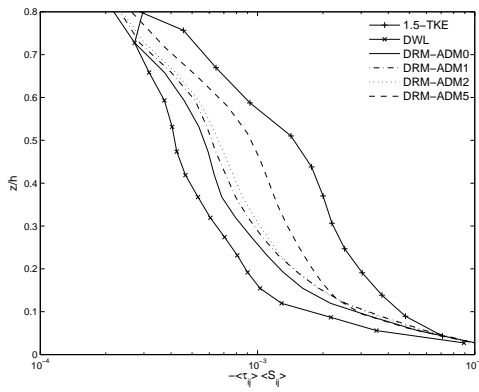


Figure 3: Vertical profile of SFS dissipation.

rally allow for backscatter from high to low wavenumbers, which is clearly desirable for sustaining turbulence in SBL simulations. This is especially true when simulating high cooling cases where sporadic bursts of turbulence are an important mixing mechanism.

Figure 3 compares the horizontally averaged SFS dissipation rate with TKE-1.5, DWL, and the DRM with four different levels of RSFS reconstruction (with clipping at zero for the DWL SGS model). We observe that the reconstruction models are far less dissipative than the TKE-1.5 model, as expected, since the RSFS stresses allow backscatter. We also notice that Π increases with higher levels of reconstruction. This happens when eddies with higher wavenumbers towards the filter cutoff are restored under more reconstruction. Interactions between these relatively high wavenumber eddies tend to generate subfilter scale motions that dissipate energy.

A further step is taken to quantify the Π probability distribution with different turbulence models by calculating statistics over a horizontal plane at a height of 30 m above ground level in Fig. 4. Neither the TKE-1.5 model, nor the DWL model (clipping eddy viscosity to zero whenever it becomes negative), has any backscatter (Π is always positive), as expected. The reconstruction models have similar peak values as the DWL model, but their dissipation distribution (positive Π) is more spread out. In other words, a more extended range of turbulent dissipation events, including occasional large values, are allowed and captured by DRM. Occurrence of backscatter events (negative Π) for DRM models accounts for roughly 10% of Π at this elevation. A slight decrease of percentage backscatter is found with higher levels of reconstruction.

The vertical distribution of the Π PDF for the DRM closures is shown in Fig. 5. In general, the distribution of Π becomes narrower, with both mean and standard deviation decreasing with height. This corresponds to the fact that most of the energy is dissipated near the ground where the most energetic turbulent motions occur. While backscatter events increase both in frequency and intensity, extreme dissipation

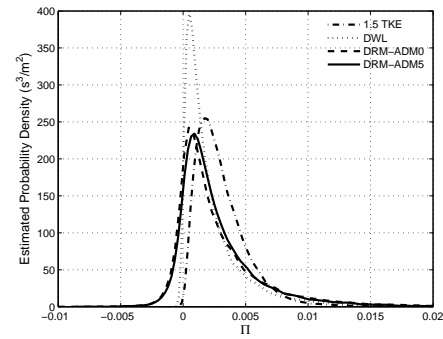


Figure 4: Probability density function (PDF) of SFS dissipation rate $p(\Pi)$ at 30 m above the ground.

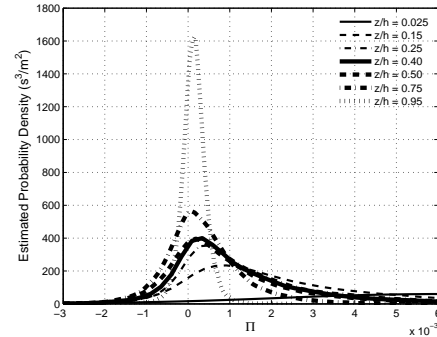


Figure 5: Probability density function $p(\Pi)$ at 7 vertical levels, case DRM-ADM5.

events become more infrequent as the SBL height is approached. There is also strong similarity observed for the normalized PDFs in the surface region of the SBL, ranging from $z/h = 0.15$ to $z/h = 0.5$.

The percentage backscatter as a function of height is plotted in Fig. 6 using 1600 samples/elevation and 20 consecutive samples. The percentage backscatter at first increases almost linearly with height, then it decreases and reaches a minimum value at the SBL depth, where turbulence is most strongly suppressed. Above the SBL height, the percentage of backscatter increases again. This supports possible turbulence generation above the SBL (see next section), where an increased number of smaller eddies join to form larger ones. Backscatter percentage decreases slightly with higher levels of reconstruction throughout the SBL (not shown), and tends to increase with higher cooling rate. Backscatter is essential in sustaining resolved-scale turbulent fluctuations at high cooling rates, because it reduces the net SFS energy drain from the resolved scales.

Low-level jet and elevated TKE

The LLJ can be defined as a thin stream of fast moving air with wind speeds of 10 to 20 m/s usually located 100 to 300 m above the ground. The LLJ is often associated with strong shear above the maximum or “nose” of the jet. Under strong stable stratification,

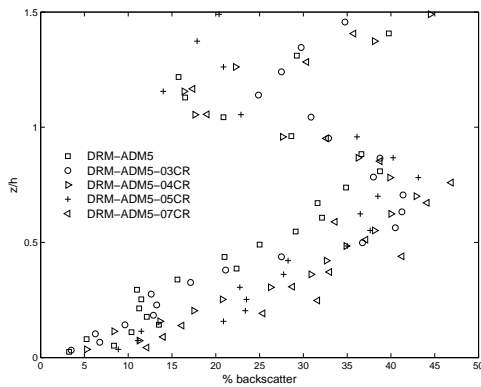


Figure 6: Vertical profile of percentage backscatter for different cooling rates.

wind shear maxima are found near the low-level jet (often occurring at wind turbine hub heights) rather than at the ground.

In a classic SBL, turbulence is generated at the surface; momentum and buoyancy fluxes decrease with height and vanish near the boundary layer top. In a non-classic SBL, turbulence generated by a LLJ often has been observed to have minimum but non-zero TKE at the level of the wind maximum, with elevated turbulence extending to two or three times above the boundary layer height. Thus, apart from the surface, turbulence is also generated above the LLJ (due to strong shear) and transported downwards, as indicated by negative vertical transport of vertical velocity variance ($\langle w'^3 \rangle$) below the jet nose (not shown, see Mahrt and Vickers, 2002). The non-classic structure is referred to as an “upside-down boundary layer”, indicating an upside-down TKE profile as compared to the traditional structure. Turbulence above the LLJ has been observed in several field campaigns (Smedman et al., 1993; Conangla and Cuxart, 2006; Cuxart and Jiménez, 2007; Mahrt and Vickers, 2002; Banta et al., 2006).

The normalized vertical TKE profile obtained using explicit filtering and the DRM is plotted in Fig. 7(a). Two peaks, one at the surface, and a smaller one around the SBL top are observed. The elevated peak with DRM indicates the presence of LLJ-generated turbulence around the SBL top, indicating that the upper and lower part of the LLJ are not completely decoupled, and that some heat and mass exchange are still possible through the LLJ by turbulent transport. In contrast, TKE obtained from the TKE-1.5 model in Fig. 7(b) shows a classic profile, single peaked near the surface and dropping to zero above. Cuxart and Jiménez (2007) found TKE above the jet nose using a TKE-1.5 model, but this was an increase in *resolved* TKE likely due to the prescribed external forcing and thus not directly comparable to our elevated subfilter-scale TKE.

As the cooling rate increases, we observe a transition from the classic to non-classic vertical TKE pro-

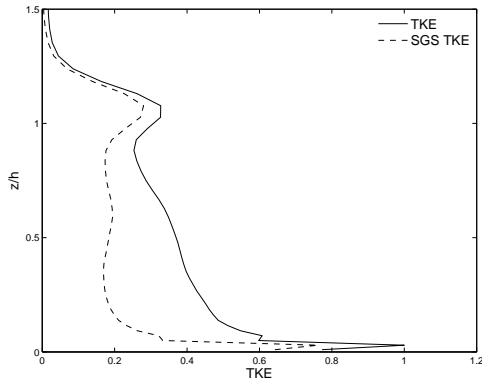
file. In Fig. 8(a), the TKE profile with a surface heat flux of -0.02 and -0.03 Km s^{-1} shows a surface maximum. A shift to the “upside-down” boundary layer profile is evident when the heat flux exceeds -0.05 Km s^{-1} . TKE is largest in the upper SBL and decreases near the surface, because strong cooling at the surface severely suppresses shear production. The mean vertical shear profile in Fig. 8(b) provides more insight into the TKE profile transition. At high cooling rates, mean shear increases significantly in the region $z/h = 0.3-0.7$, where we observe the enhanced TKE in Fig. 8(a). The overall elevated TKE profile obtained at heat flux -0.07 Km s^{-1} agrees well both qualitatively and quantitatively with the field observations from the CASES-99 experiment (see Fig. 7 of Pichugina and Banta, 2009).

The dynamic reconstruction models are able to capture the elevated TKE due to the filtering and reconstruction procedure. In particular, the 3D reconstruction process accounts for any vertical gradient in the filtered horizontal velocity field (\tilde{u}, \tilde{v}), such that $\tau_{RSFS,ii}$ is an explicit function of $\partial \tilde{u}_i / \partial z$. Strong vertical shear around the LLJ thus contributes to the normal stresses (in x , for example, $\partial \tilde{u} / \partial z$ contributes directly to τ_{11}). The contribution of *vertical* gradients of the horizontal velocity on the normal stresses is not included in eddy-viscosity models (e.g. $\partial u / \partial z$ contributes to τ_{13} but not τ_{11}). Even the TKE-1.5 closure cannot capture this elevated TKE, because strong stratification damps TKE production in the TKE equation due to limitations of the eddy-viscosity closures used within.

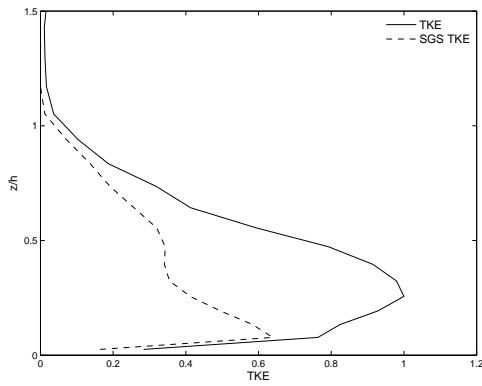
The elevated TKE found in the DRM model is thus contributed by the RSFS terms through vertical filtering and subsequent reconstruction. This is confirmed by performing another simulation with exactly the same setup of DRM-ADM5, but without vertical filtering (just 2D horizontal filtering). While the overall simulation results are similar to DRM-ADM5, the vertical TKE profile changes back into a classic picture of the surface maximum case (Fig. 7(c)). The SFS TKE decreases to zero at $z/h = 1$, which confirms our observation of the importance of vertical filtering and reconstruction to capture the elevated TKE.

6 Summary and conclusions

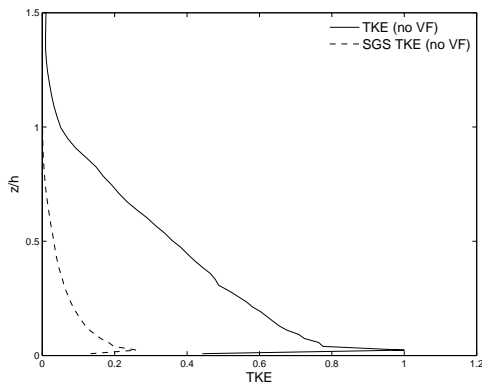
To achieve optimum turbine micrositing and obtain reliable estimates of wind resources, accurate predictions of wind speed and turbulence in the near-surface boundary layer are required. This study performed LES of the stably stratified atmospheric boundary layer using the explicit filtering framework and dynamic reconstruction turbulence model of Chow et al. (2005) to capture atmospheric dynamics that do not conform to traditional assumptions of gradient-diffusion turbulence models. A quasi-steady state SBL was simulated with sustained turbulence, even under stronger cooling scenarios. The



(a)

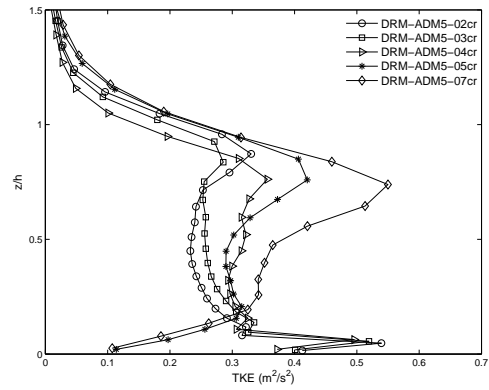


(b)

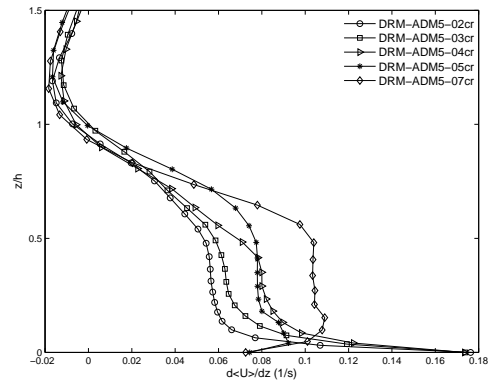


(c)

Figure 7: Normalized vertical profile of TKE, total (solid) and SFS (dashed). (a) case DRM-ADM5, (b) case TKE-1.5, (c) case DRM-ADM5, without vertical filtering



(a)



(b)

Figure 8: Vertical profile of (a) TKE and (b) mean shear for different cooling rates, case DRM-ADM5.

explicit filtering and dynamic reconstruction model demonstrated superior performance compared to conventional eddy-viscosity models, even at coarser resolutions than typically recommended for SBL simulations.

Our LES model applies an explicit filtering procedure to the governing flow equations which separates the turbulent stress into resolvable subfilter scales (RSFS) and subgrid scales (SGS). An anisotropic tophat filter is used to define the RSFS stress, which can be reconstructed using an iterative filter inversion procedure. The RSFS stress is ignored in the traditional LES approach but provides valuable information about the nature of turbulent interactions near the grid cutoff for numerical schemes based on finite volumes or finite differences. The SGS portion is modeled with a dynamic eddy-viscosity model with a near-wall stress augmentation. The RSFS/SGS explicit filtering and reconstruction procedure proves to be advantageous for SBL simulations because the RSFS portion effectively represents intermittent turbulence by allowing energy backscatter.

Simulation with the DRM predicts more realistic mean wind speed and temperature profiles under stable conditions. In comparison, conventional eddy viscosity models tend to produce a shallow mixing layer under moderately stable conditions, and eventually lami-

nar flow under strong stability. DRM models also predict a higher shear exponent than the IEC specification under stable conditions. This supports the observed high positive correlation between turbine fault time and shear exponent at wind farms in the US Southern Great Plains region, suggesting that better guidelines are required for turbine design and operation under stable stratification.

In terms of vertical shear profiles, we observed general agreement with Monin-Obukhov similarity and Businger-Dyer flux profile relationships (Businger et al., 1971) in the surface layer, even at relatively coarse resolutions. Under strong cooling conditions, non-dimensional shear profiles remain linear but deviations from MO similarity theory become larger as cooling is increased. There is no consensus in the literature about whether MO theory is valid under strong cooling conditions. A further step was taken to quantify LES dissipation and backscatter with DRM. Extreme dissipation events become more infrequent as the SBL height is approached, while backscatter events increase both in frequency and intensity. Backscatter percentages showed a slight decrease with increasing levels of reconstruction and an increase with stronger cooling rates. The ability of LES turbulence closures to represent backscatter may affect prediction of intermittent shear and turbulence events that are of interest in wind turbine design and operation.

A non-classic SBL structure developed in our simulations due to the presence of a low-level jet. Wind shear in the LLJ generates turbulence, thus the vertical TKE structure revealed two peaks. The near surface region followed the classic SBL structure with a surface maximum of TKE. Around the top of the SBL, turbulence generation by the LLJ resulted in another peak in TKE profile. The vertical TKE profile transitioned from the classic surface maximum to the non-classic “upside-down” case with elevated TKE as surface cooling was increased, which compare well with observations from CASES-99. The DRM is uniquely able to capture the elevated TKE due to the 3D explicit filtering that accounts for vertical gradients of horizontal velocities even in the normal stresses. Furthermore, we observed that the presence of LLJ intensified vertical shear that extends to as high as 70% of the boundary layer height in strongly cooled conditions. Regions of elevated TKE and high shear need to be accurately represented to reduce wind turbine fault time and turbine fatigue.

In conclusion, we have demonstrated the ability of explicit filtering and dynamic reconstruction models to successfully simulate the boundary layer under stable conditions. LES with DRM is capable of covering a wide range of stability conditions, extending into the intermittent turbulence regime where traditional LES closures usually fail. The approach described has the advantage that almost any existing SGS model can be adapted to an explicit filtering and re-

construction framework. This is achieved most simply by adding a scale similarity component (RSFS) to existing SGS closures (see Chow and Street, 2009; Chow et al., 2005). Using LES with DRM closures as a tool for SBL simulations, we expect to maximize wind power production by providing accurate vertical wind speed profiles, and minimize turbine fatigue and fault time by predicting potentially high shear and turbulence events around turbines.

Acknowledgments

We are grateful for support from National Science Foundation Grant ATM-0645784 (Program Director S. Nelson of the Physical and Dynamic Meteorology Program). Acknowledgment is also made to the National Center for Atmospheric Research, which is sponsored by NSF, for the computing time used in this research.

References

- Banta, R. M., Y. L. Pichugina, and W. A. Brewer, 2006: Turbulent velocity-variance profiles in the stable boundary layer generated by a nocturnal low-level jet. *Journal of the Atmospheric Sciences*, **63** (11), 2700–2719.
- Bardina, J., J. Ferziger, and W. Reynolds, 1983: Improved turbulence models based on large eddy simulation of homogeneous, incompressible, turbulent flows. *Tech. Rep. TF-19. Department of Mechanical Engineering*, 97pp.
- Basu, S. and F. Porté-Agel, 2006: Large-eddy simulation of stably stratified atmospheric boundary layer turbulence: A scale-dependent dynamic modeling approach. *Journal of the Atmospheric Sciences*, **63** (8), 2074–2091.
- Basu, S., J. Vinuesa, and A. Swift, 2008: Dynamic LES modeling of a diurnal cycle. *Journal of Applied Meteorology and Climatology*, **47** (4), 1156–1174, doi: 10.1175/2007JAMC1677.1.
- Beare, R., et al., 2006: An intercomparison of large-eddy simulations of the stable boundary layer. *Boundary-Layer Meteorology*, **118** (2), 247–272, doi:10.1007/s10546-004-2820-6.
- Bechmann, A. and N. Sorensen, 2010: Hybrid RANS/LES method for wind flow over complex terrain. *WIND ENERGY*, **13** (1), 36–50, doi:10.1002/we.346.
- Brown, A., J. Hobson, and N. Wood, 2001: Large-eddy simulation of neutral turbulent flow over rough sinusoidal ridges. *Boundary-Layer Meteorology*, **98** (3), 411–441.
- Businger, J., J. Wyngaard, Y. Izumi, and E. Bradley, 1971: Flux-profile relationships in atmospheric surface layer. *Journal of the Atmospheric Sciences*, **28** (2), 181–&.
- Calaf, M., C. Meneveau, and J. Meyers, 2010: Large eddy simulation study of fully developed wind-turbine array boundary layers. *Physics of Fluids*, **22** (1), doi: 10.1063/1.3291077.
- Carper, M. and F. Porté-Agel, 2004: The role of coherent structures in subfilter-scale dissipation of turbulence measured in the atmospheric surface layer. *Journal of Turbulence*, **5**, doi:10.1088/1468-5248/5/1/040.
- Cederwall, R. T., 2001: Large-eddy simulation of the evolving boundary layer over flat terrain. Ph.D. thesis, Stanford University.

- Chow, F., R. Street, M. Xue, and J. Ferziger, 2005: Explicit filtering and reconstruction turbulence modeling for large-eddy simulation of neutral boundary layer flow. *Journal of the Atmospheric Sciences*, **62** (7), 2058–2077.
- Chow, F. K. and R. L. Street, 2009: Evaluation of Turbulence Closure Models for Large-Eddy Simulation over Complex Terrain: Flow over Askervein Hill. *Journal of Applied Meteorology and Climatology*, **48** (5), 1050–1065, doi:10.1175/2008JAMC1862.1.
- Conangla, L. and J. Cuxart, 2006: On the turbulence in the upper part of the low-level jet: An experimental and numerical study. *Boundary-Layer Meteorology*, **118** (2), 379–400, doi:10.1007/s10546-005-0608-y.
- Cuxart, J. and M. A. Jiménez, 2007: Mixing processes in a nocturnal low-level jet: An LES study. *Journal of the Atmospheric Sciences*, **64** (5), 1666–1679, doi:10.1175/JAS3903.1.
- Gullbrand, J. and F. Chow, 2003: The effect of numerical errors and turbulence models in large-eddy simulations of channel flow, with and without explicit filtering. *Journal of Fluid Mechanics*, **495**, 323–341, doi:10.1017/S0022112003006268.
- Kelley, N. D., B. J. Jonkman, and G. N. Scott, 2006: The Great Plains turbulence environment: its origins, impact and simulation. Tech. Rep. NREL/CP-500-40176, National Renewable Energy Laboratory, Golden, CO.
- Kirkpatrick, M., A. Ackerman, D. Stevens, and N. Mansour, 2006: On the application of the dynamic Smagorinsky model to large-eddy simulations of the cloud-topped atmospheric boundary layer. *Journal of the Atmospheric Sciences*, **63** (2), 526–546.
- Lilly, D. K., 1992: A proposed modification of the Germano subgrid-scale closure method. *Physics of Fluids A-Fluid Dynamics*, **4** (3), 633–635.
- Lund, T. S., 1997: On the use of discrete filters for large eddy simulation. Tech. rep., Center for Turbulence Research, NASA Ames-Stanford University, 83-95 pp.
- Mahrt, L. and D. Vickers, 2002: Contrasting vertical structures of nocturnal boundary layers. *Boundary-Layer Meteorology*, **105** (2), 351–363.
- Mason, P. and S. Derbyshire, 1990: Large-eddy simulation of the stably-stratified atmospheric boundary-layer. *Boundary-Layer Meteorology*, **53** (1-2), 117–162.
- Paiva, L., G. Bodstein, and W. Menezes, 2009: Numerical simulation of atmospheric boundary layer flow over isolated and vegetated hills using RAMS. *Journal of Wind Engineering and Industrial Aerodynamics*, **97** (9-10), 439–454.
- Palma, J., F. Castro, L. Ribeiro, A. Rodrigues, and A. Pinto, 2008: Linear and nonlinear models in wind resource assessment and wind turbine micro-siting in complex terrain. *Journal of Wind Engineering and Industrial Aerodynamics*, **96** (12), 2308–2326, doi:10.1016/j.jweia.2008.03.012.
- Pichugina, Y. and R. Banta, 2009: Stable boundary-layer depth from high-resolution measurements of the mean wind profile. *Journal of Applied Meteorology and Climatology*, **49** (1), 20–35.
- Saiki, E., C. Moeng, and P. Sullivan, 2000: Large-eddy simulation of the stably stratified planetary boundary layer. *Boundary-Layer Meteorology*, **95** (1), 1–30.
- Sisterson, D. and P. Frenzen, 1978: Nocturnal boundary-layer wind maxima and problem of wind power assessment. *Environmental Science & Technology*, **12** (2), 218–221.
- Smedman, A., M. Tjernstrom, and U. Hogstrom, 1993: Analysis of the turbulence structure of a marine low-level jet. *Boundary-Layer Meteorology*, **66** (1-2), 105–126.
- Smith, K., G. Randall, N. Kelley, and B. Smith, 2002: Evaluation of wind shear patterns at midwest wind energy facilities. *Proceedings American Wind Energy Association (AWEA) Windpower 2002 Conference*.
- Stolz, S., N. Adams, and L. Kleiser, 2001: The approximate deconvolution model for large-eddy simulations of compressible flows and its application to shock-turbulent-boundary-layer interaction. *Physics of Fluids*, **13** (10), 2985–3001.
- Storm, B., J. Dudhia, S. Basu, A. Swift, and I. Giammanco, 2009: Evaluation of the weather research and forecasting model on forecasting low-level jets: Implications for wind energy. *Wind Energy*, **12** (1), 81–90, doi:10.1002/we.288.
- Sullivan, P., J. McWilliams, and C. Moeng, 1994: A subgrid-scale model for large-eddy simulation of planetary boundary-layer flows. *Boundary-Layer Meteorology*, **71** (3), 247–276.
- Wilson, J. D., 2008: Monin-Obukhov Functions for Standard Deviations of Velocity. *Boundary-Layer Meteorology*, **129** (3), 353–369, doi:10.1007/s10546-008-9319-5.
- Wong, V. and D. Lilly, 1994: A comparison of 2 dynamic subgrid closure methods for turbulent thermal convection. *Physics of Fluids*, **6** (2), 1016–1023.
- Xue, M., K. Droegemeier, and V. Wong, 2000: The Advanced Regional Prediction System (ARPS) - A multi-scale nonhydrostatic atmospheric simulation and prediction model. Part I: Model dynamics and verification. *Meteorology and Atmospheric Physics*, **75** (3-4), 161–193.
- Zang, Y., R. Street, and J. Koseff, 1993: A dynamic mixed subgrid-scale model and its application to turbulent recirculation-flows. *Physics of Fluids A-Fluid Dynamics*, **5** (12), 3186–3196.